

1 Comparison of modeled and observed effects of
2 radiation belt electron precipitation on mesospheric
3 hydroxyl and ozone

Pekka T. Verronen,¹ Monika E. Andersson,¹ Craig J. Rodger,²

Mark A. Clilverd,³ Shuhui Wang,⁴ and Esa Turunen⁵

P. T. Verronen, M. E. Andersson, Earth Observation, Finnish Meteorological Institute, P.O. Box 503, FI-00101 Helsinki, Finland. (pekka.verronen@fmi.fi, monika.andersson@fmi.fi)

C. J. Rodger, Department of Physics, University of Otago, P.O. Box 56, Dunedin, New Zealand. (crodger@physics.otago.ac.nz)

M. A. Clilverd, British Antarctic Survey (NERC), High Cross, Madingley Road, Cambridge CB3 0ET, UK. (macl@bas.ac.uk)

S. Wang, Jet Propulsion Laboratory, 4800 Oak Grove Drive, Pasadena, CA 91109, USA. (shuhui.wang@jpl.nasa.gov)

E. Turunen, Sodankylä Geophysical Observatory, Tähteläntie 62, FI-99600 Sodankylä, Finland. (esa.turunen@sgo.fi)

¹Earth Observation, Finnish

4 **Abstract.** Observations have shown that mesospheric hydroxyl (OH) is
5 affected by energetic electron precipitation (EEP) at magnetic latitudes con-
6 nected to the outer radiation belt. It is not clear, however, if the current satellite-
7 based electron flux observations can be used to accurately describe EEP in
8 atmospheric models. We use the Sodankylä Ion and Neutral Chemistry (SIC)
9 model to reproduce the changes in OH and ozone observed by the Microwave
10 Limb Sounder (MLS/Aura) during four strong EEP events. The daily mean
11 electron energy-flux spectrum, needed for ionization rate calculations, is de-
12 termined by combining the Medium Energy Proton and Electron Detector
13 (MEPED/POES) fluxes and spectral form from the IDP high-energy elec-
14 tron detector on board the DEMETER satellite. We show that in general

Meteorological Institute, Helsinki, Finland

²Department of Physics, University of
Otago, Dunedin, New Zealand

³British Antarctic Survey (NERC),
Cambridge, UK

⁴Jet Propulsion Laboratory, California
Institute of Technology, Pasadena,
California, USA

⁵Sodankylä Geophysical Observatory,
University of Oulu, Sodankylä, Finland

15 SIC is able to reproduce the observed day-to-day variability of OH and ozone.
16 In the lower mesosphere, the model tends to underestimate the OH concen-
17 tration, possibly because of uncertainties in the electron spectra for energies
18 >300 keV. The model predicts OH increases at 60–80 km, reaching several
19 hundred percent at 70–80 km during peak EEP forcing. Increases in OH are
20 followed by ozone depletion, up to several tens of percent. The magnitude
21 of modeled changes is similar to those observed by MLS, and comparable to
22 effects of individual solar proton events. Our results suggest that the com-
23 bined satellite observations of electrons can be used to model the EEP ef-
24 fects above 70 km during geomagnetic storms, without a need for significant
25 adjustments. However, for EEP energies >300 keV impacting altitudes <70 km,
26 correction factors may be required.

1. Introduction

27 The odd hydrogen family ($\text{HO}_x = \text{H} + \text{OH} + \text{HO}_2$) plays an important role in the meso-
28 spheric O_3 balance by participating in catalytic ozone-destroying reactions, and in reac-
29 tions between different forms of other ozone depleting compounds. However, continuous
30 satellite observations of OH and HO_2 became available less than ten years ago, after the
31 launch of the Microwave Limb Sounder (MLS/Aura) instrument in 2004 [*Pickett et al.*,
32 2008]. In the mesosphere, the primary HO_x production mechanism is photodissociation of
33 water vapor by solar radiation ($\lambda < 200$ nm) and its loss is due to "cannibalistic" reactions
34 such as $\text{OH} + \text{HO}_2 \rightarrow \text{H}_2\text{O} + \text{O}_2$. The OH concentration increases by roughly an order
35 of magnitude during daytime, except in a narrow layer around 82 km where a reaction
36 between ozone and atomic hydrogen creates a nighttime OH maximum [*Pickett et al.*,
37 2006]. In the polar regions, enhancements of HO_x occur during energetic particle precipi-
38 tation events, when increases in ionization rates lead to odd hydrogen production through
39 ionization and water cluster ion chemistry [*Heaps, 1978; Solomon et al., 1981; Verronen*
40 *and Lehmann, 2013*]. Large changes are caused by solar proton events (SPE), during
41 which high fluxes of highly energetic protons, related to coronal mass ejections from Sun,
42 can affect the mesosphere and upper stratosphere for several days. For example, in the
43 case of the January 2005 SPE, order-of-magnitude OH increases have been observed at
44 60–80 km, with subsequent decreases in ozone by 50–90% [*Verronen et al., 2006; Damiani*
45 *et al., 2008*]. Energetic particle precipitation can increase HO_x below about 80 km, where
46 there is enough H_2O for water cluster ion formation. At these altitudes, the nighttime
47 background concentration of HO_x is low and its chemical lifetime varies between 0.1 and

48 1 day [e.g. *Pickett et al.*, 2006]. This means that HO_x is a useful monitor species for
49 short-term precipitation variations, because its concentration responds rapidly to both
50 increases and decreases in particle forcing [*Damiani et al.*, 2010; *Verronen et al.*, 2011].

51 Recent observational studies using data from the Medium Energy Proton and Electron
52 Detector (MEPED/POES) and Microwave Limb Sounder (MLS/Aura) have shown that
53 radiation belt electrons, precipitating into the atmosphere during magnetic storms, have a
54 significant effect on mesospheric nighttime hydroxyl concentrations at magnetic latitudes
55 between 55° and 72°. *Verronen et al.* [2011] studied two months, March 2005 and April
56 2006, and found a significant correlation between electron count rates and hydroxyl in both
57 hemispheres providing some of the first experimental evidence that electron precipitation
58 could produce significant HO_x changes. Electron precipitation was shown to cause day-to-
59 day OH changes up to 100% and explain 56–87% of the OH variability. *Andersson et al.*
60 [2012] extended the correlation study and analyzed 65 months between 2004 and 2009.
61 In about 34% of the time, they found a clear correlation between electron counts and
62 hydroxyl concentrations. In both studies, the largest OH response was seen at 70–78 km
63 altitude, while below 50 km and above 80 km no correlation was found.

64 The relation between the electron counts measured in the radiation belts and the pre-
65 cipitating electron fluxes is in many cases not trivial, because satellite instruments, such
66 as MEPED/POES, typically measure only a fraction of the precipitation and the electron
67 measurements can be contaminated by protons [*Rodger et al.*, 2010a]. Recent studies using
68 ground-based measurements have indicated that an adjustment of >30 keV electron fluxes,
69 up to a factor of 10, may be needed in order to produce the observed ionospheric response
70 in models [*Hendry et al.*, 2012; *Clilverd et al.*, 2012]. However, because the ground-based

71 instruments used in these studies can monitor an altitude-integrated response only, it is
72 not clear if the required adjustment depends on electron energy. On the other hand, it is
73 increasingly likely that an adjustment is needed for electron energies >300 keV. Accord-
74 ing to radiation belt models (R.B. Horne, private communication), when electron energy
75 increases towards MeV level there is increasingly uneven effect of wave-particle scattering
76 on the bounce loss cone (BLC). This means that the distribution of electrons with a given
77 energy changes inside the BLC. As a result, a satellite instrument sampling only a fraction
78 of the BLC, such as MEPED, is likely to miss a larger part of precipitating electrons at
79 high energies.

80 In this paper, we use the Sodankylä Ion and Neutral Chemistry (SIC) model to study
81 the effect of precipitating radiation belt electrons on mesospheric OH and O₃. The electron
82 spectra input to the model was calculated using flux observations of MEPED/POES and a
83 power-law form previously found to be appropriate using data from the IDP (Instrument
84 for the Detection of Particles) high-energy electron detector on board the DEMETER
85 (Detection of Electro-Magnetic Emissions Transmitted from Earthquake Regions) micro
86 satellite [*Chilverd et al.*, 2010]. A detailed comparison between the model results and
87 OH observations from MLS/Aura allows us to test the quality of the electron spectra at
88 different electron energies.

2. Modeling, Measurements, and Comparison

89 Between 2004 and 2009, there were several energetic electron precipitation (EEP) events
90 which had a clear effect on mesospheric hydroxyl [*Andersson et al.*, 2012]. In this work
91 we consider four of the strongest events that occurred during this time period: January,
92 March, May 2005 and April 2006. These events were selected to provide the most de-

93 tectable electron forcing on the middle atmosphere, and thus, are best suited for our
94 purpose of testing the quality of the satellite-based electron fluxes. Also, these time peri-
95 ods are not affected by SPEs, during which the electron flux measurements are corrupted
96 by protons [Rodger *et al.*, 2010a].

2.1. Sodankylä Ion and Neutral Chemistry model

97 The Sodankylä Ion and Neutral Chemistry model is a one-dimensional tool designed for
98 ionospheric and middle atmospheric studies. The latest version solves the concentrations
99 of 65 ions, including 29 negative ions and 16 neutral species between 20–150 km altitude (1-
100 km resolution). A chemical scheme of about 400 reactions is included (including standard
101 O_x , HO_x , and NO_x neutral chemistry), as well as external forcing by solar UV-VIS and
102 soft X-ray radiation, electron and proton precipitation, and galactic cosmic rays. In this
103 study, the temporal resolution was selected to be 15 minutes. A more detailed description
104 of SIC is given elsewhere [Verronen *et al.*, 2005; Verronen, 2006; Turunen *et al.*, 2009].

105 Considering the effects of electron precipitation, in the SIC model the calculation of
106 ionization rates uses an experimental energy dissipation function and energy–range rela-
107 tion for electrons, see Rees [1989, Chapter 3.3] for more details. The dissipation function
108 assumes an isotropic angular distribution, and the range of electrons is calculated using
109 the expression given by Goldberg *et al.* [1984]. The chemical production of HO_x species
110 in the model, after ionization takes place, involves dissociation of H_2O , water cluster ion
111 formation through positive ion chemistry, and recombination processes which lead to OH
112 and H production [Verronen and Lehmann, 2013]. The produced HO_x then affects ozone
113 in the mesosphere through the well-known catalytic reaction cycles of neutral chemistry
114 [e.g. Grenfell *et al.*, 2006].

115 The ionization rate calculation requires an energy-flux spectrum of electrons. In
116 construction of the spectra, we combined observations from two satellite instruments:
117 MEPED/POES and IDP/DEMETER [*Evans and Greer, 2004; Sauvaud et al., 2006*].
118 MEPED observations are available for three energy threshold channels, >30 keV,
119 >100 keV, and >300 keV, from three different POES satellites. We utilized data from
120 magnetic latitudes $55 - 65^\circ$ (McIlwain L shells 3.0–5.7) gathered by the 0° detector, which
121 points radially outwards along the Earth-satellite direction and measures count rates of
122 precipitating radiation belt electrons [*Rodger et al., 2010a; Rodger et al., 2010b*]. Follow-
123 ing the previous work in this area [*Verronen et al., 2011; Andersson et al., 2012; Hendry*
124 *et al., 2012*], we exclude fluxes from the South Atlantic region, where the instrument is
125 contaminated by high-energy protons. We then calculated daily zonal mean of the electron
126 fluxes for the three MEPED energy channels, and used them to fit an energy spectrum.
127 The spectral form of the fit is based on the power-law relationship previously found to
128 be appropriate using observations of the IDP instrument [*Clilverd et al., 2010*]. IDP has
129 128 energy channels and thus a vastly better energy resolution compared to the three
130 integral channels from MEPED. However, IDP does not measure precipitating electrons
131 but electrons in the drift loss cone, i.e., electrons that have a pitch angle close to the
132 precipitation limit but which drift around the Earth to be lost where the magnetic field
133 is weakest (in the South Atlantic). Therefore, our assumption is that the precipitating
134 electrons have same spectral form as those in the drift loss cone, as they are very close in
135 pitch angle space.

136 Fig. 1 shows examples of electron energy spectra (left panel) and ionization rates (right
137 panel) for three different days in January 2005: before (1 January), during (2 January)

138 and after (3 January) an EEP event. The flux on 2 January exceeds the 1 January flux by
 139 almost two orders of magnitude at the lower energies, while at the highest energies there
 140 is an increase by a factor of three. When the electron flux peaks, ionization rates are
 141 about 10 times higher than the values before the peak EEP, with the maximum increase
 142 between 70–100 km. It is important to note that the atmospheric penetration depth of
 143 an electron depends on its energy [e.g. *Turunen et al.*, 2009, Fig. 3]. As shown in Fig. 1,
 144 the calculated ionization rate is always zero below 50 km because we do not consider
 145 electrons with energies larger than 2000 keV, which would penetrate to stratospheric
 146 altitudes. This upper energy limit is set by the MEPED and IDP measurements, because
 147 both instruments respond to electron energies less than about 2500 keV only [*Evans and*
 148 *Greer*, 2004]. The lower limit of electron energy is set at 50 keV in order to capture the
 149 EEP effect at altitudes below about 90 km.

150 The times and locations of the model runs are given in Table 1. For each of the
 151 four cases, the SIC model was run for two geographic locations, one in the northern
 152 hemisphere (NH) and one in the southern hemisphere (SH). These locations are at about
 153 60°N/S geomagnetic latitude, which connects to the center of the outer radiation belt via
 154 magnetic field lines. For each location/month, two model runs were made: 1) an EEP
 155 run with the observed, daily-average EEP forcing, and 2) a CTR (control) run with low
 156 and constant EEP forcing corresponding to quiet-time conditions (defined as the average
 157 of 3–4 March, 2005). MLS/Aura observations of water vapor (H₂O) and temperature
 158 (T), monthly-averaged for each case separately, were used in the SIC modeling to provide
 159 more realistic atmospheric conditions. The rest of the background neutral atmosphere and
 160 daily solar flux spectrum were generated using the MSISE-90 and the SOLAR2000 models,

161 respectively [*Hedin, 1991; Tobiska et al., 2000*]. To make the model results and satellite
162 measurements comparable, OH and O₃ altitude profiles from SIC were interpolated to
163 the logarithmic pressure grid of MLS observations. Then, the MLS averaging kernel was
164 applied to O₃ profiles from SIC to compensate for the coarser vertical resolution of the MLS
165 observations [see *Livesey et al., 2011*, for more details]. The vertical resolution of MLS
166 OH observations is closer to the 1-km model resolution, i.e. 2.5 km at all altitudes below
167 80 km, and thus the OH averaging kernel was not applied to model results because its
168 effect would be small. Note that the results are presented on a vertical grid of approximate
169 altitudes, which correspond to the pressure levels of the MLS observations.

2.2. Observations of Hydroxyl and Ozone

170 The MLS instrument on board the Aura satellite was launched in July 2004 [*Waters*
171 *et al., 2006*]. The Aura satellite is in a high-inclination orbit, and the MLS observations
172 cover the polar regions (geographic latitudes less than 82°). Detailed information on the
173 MLS OH and O₃ products can be found elsewhere [*Pickett et al., 2008; Jiang et al., 2007;*
174 *Livesey et al., 2011*]. We use Version 3.3 Level 2 nighttime (solar zenith angle $\geq 100^\circ$)
175 data from geomagnetic latitudes 59–65° from both hemispheres. At these latitudes, MLS
176 nighttime observations correspond to local times of 22:00–02:00 and 02:00–03:30 in the
177 SH and NH, respectively. Before the analysis, the data were screened according to the
178 MLS data description and quality document [*Livesey et al., 2011*]. We then calculated
179 nightly zonal averages and corresponding SEMs (standard error of the mean) at each
180 pressure level of MLS observations. The number of individual profiles used in calculating
181 the means varied between 100 (NH) in January to 15 (NH) in May (see Table 1). Due
182 to the incomplete nighttime zonal coverage in January SH and May NH, the longitudinal

183 range was limited to 0–180° E and 0–180° W, respectively. For these two cases, the model
184 runs were made at 50°S/105°E (January) and at 55°N/75°W (May), according to the
185 radiation belt position at these longitudes.

186 We have chosen to work with daily zonal averages instead of a finer temporal and spatial
187 resolution. This approach reduces uncertainties of the observational data to an acceptable
188 level but, on the other hand, it restricts us from fine-detail comparisons between the SIC
189 model and MLS observations. However, since the aim is to understand if large corrections
190 (e.g. scaling factors of 10) are needed for the electron flux data, the current approach is
191 appropriate for this study. For a given geographic latitude, the MLS observations have
192 the same local solar time (LST) at all longitudes. So, daily zonal averages only include
193 observations of about the same LST (the LST range depending on the latitude range
194 selection). Because we force the model with daily zonal mean electron fluxes, the model
195 results at different longitudes (but sampled at the same LST) would not be significantly
196 different. Thus the model results from one longitude are comparable to the daily zonal
197 mean of MLS observations. Note that HO_x production is nearly linear with respect to
198 particle ionization rate (although the HO_x production efficiency does decrease slowly with
199 increasing ionization, see e.g. *Verronen and Lehmann* [2013]), which means that the daily
200 average ionization rates produce a modeled OH result that should be very similar to daily
201 average OH results produced using a finer temporal resolution for the ionization rates.

3. Results

202 Fig. 2 shows the temporal variation of the calculated NH daily EEP ionization rates
203 at 60, 70, and 80 km. In all four cases there are substantial day-to-day variations in
204 ionization, which should lead to observable changes in mesospheric OH concentrations.

205 On quiet days the ionization rates are between 1 and $10 \text{ cm}^{-3}\text{s}^{-1}$ at all altitudes shown,
206 while the peak ionization during EEP events can exceed $10^2 \text{ cm}^{-3}\text{s}^{-1}$. For comparison, the
207 ionization by solar Lyman- α radiation and galactic cosmic rays typically varies between
208 0.1 and $10 \text{ cm}^{-3}\text{s}^{-1}$ at these altitudes, and during very large SPEs the daily average
209 ionization rate can be higher than $10^3 \text{ cm}^{-3}\text{s}^{-1}$. Therefore, the peak EEP ionization rates
210 are clearly higher than the normal background, but are still about an order of magnitude
211 lower than for the largest SPEs.

212 Fig. 3 presents a comparison between the modeled and observed EEP-related relative
213 changes of OH and O_3 at about 75 km altitude for two of the cases: January 2005/NH
214 and March 2005/SH, which represent the magnitude range of the EEP effects. For the
215 model results, the change is shown 1) between the EEP and CTR runs (red line) and
216 2) between the EEP run and the 1st-day value of the EEP run (red X marks, only for the
217 LST of MLS observations).

218 First looking at the modeled change with CTR run as a reference, the model results
219 clearly show how the relative change is dependent on local time. For example, the largest
220 OH increases are seen in the early morning hours, around sunrise, when the background
221 OH concentration is lowest. In March 2005/SH, when the noon solar zenith angle is much
222 lower than in January, the noon time OH increase is negligible, i.e. of the order of 1%.
223 Also the ozone change is dependent on the local time, its depletion taking place at sunrise
224 and sunset, when 1) HO_x concentration is elevated by EEP and 2) enough atomic oxygen
225 is available for the ozone-destroying catalytic HO_x reaction cycles (note that the sunrise
226 decrease of ozone is not always seen in Fig. 3 because a decrease in daily EEP forcing
227 from the previous day can lead to ozone recovery at sunrise). Thus the largest ozone

228 changes do not necessarily coincide with the largest OH changes. At night, no significant
229 production or loss of O_3 takes place because of the absence of solar radiation and atomic
230 oxygen. Contrary to the model results, the observations are only available at certain local
231 times, as shown in Fig. 3. In the case of OH, the model results are in general agreement
232 with the observations, predicting maximum increases that reach 80–100% at the local
233 time of the observations. However, in January/NH SIC tends to underestimate the EEP
234 impact (MLS shows increase by 165% on 2 January), and in March/SH the model is
235 overestimating the change on March 8. However, on many days the data points agree
236 or nearly agree within the SEM of the observations (shown by the error bar in Fig. 3).
237 For ozone, the modeled depletion is up to 40% and 16% in January/NH and March/SH,
238 respectively, varying from day to day with the level of EEP forcing and the related OH
239 change. The observations do show a smaller decrease in January/NH, up to 25–30% only,
240 but qualitatively the day-to-day behavior (depletion and recovery) is similar to the model
241 in both cases. Note that the SEM of the ozone observations in March/SH is larger than
242 the predicted changes.

243 When the modeled changes are shown relative to the 1st-day value (1 January and
244 5 March), in January/NH both the OH increase and ozone depletion are smaller than
245 when using CTR run as a reference. This is because the EEP ionization rates are already
246 elevated on 1 January (Fig. 2). The maximum OH increase on 2 January is 70%, which
247 is again smaller than that observed. On the other hand, the ozone change is in a better
248 agreement with MLS although still overestimated on 3 and 4 January. In March/SH, the
249 modeled OH change is not much different compared to that relative to the CTR run. The
250 ozone change is different because the day-to-day background variability is comparable to

251 that driven by EEP. In this case, the CTR run reference gives a better estimate of ozone
252 changes, because it removes the underlying day-to-day variability.

253 Fig. 4 shows the NH comparisons between SIC and MLS daily concentration profiles
254 1) before, 2) during, and 3) after the peak EEP day. In all cases, the modeled OH
255 concentrations are elevated on the peak EEP day compared to the day before, and then
256 at least partly recover on the following day. Largest effects are seen at altitudes between
257 60 and 80 km. Although there are clear differences in absolute numbers between MLS and
258 SIC at a number of altitudes, the model seems to be able to qualitatively represent most
259 of the observed day-to-day changes in OH. Table 2 presents the observed and modeled
260 NH mean OH increase from the day-before to peak-EEP concentrations at 60–70 km and
261 71–81 km. In general, SIC tends to overestimate rather than underestimate the increase
262 compared to MLS although the difference is only in tens of percent in most cases. At higher
263 altitudes, this is caused in few cases by an overestimation of the EEP effect in the model
264 (e.g. 14-Apr-2006 in Fig. 4), while at lower altitudes the difference in relative change is
265 at least partly due to lower reference concentrations (CTR) in SIC (e.g. 05-March-2005
266 in Fig. 4). On 30-May-2005 the difference between SIC and MLS is especially large, the
267 EEP model run predicting clearly larger amounts of OH than those observed. The larger
268 differences could be related to the smaller amount of MLS measurements available for this
269 month, because a nightly zonal mean calculated with limited number of available data
270 points is less representative of the rapidly changing EEP effect. As shown in Table 3,
271 on the EEP peak days the OH profiles from the EEP run agree with MLS observations
272 better than those from the CTR run, except in May 2005.

273 Fig. 5 and Table 4 present the same comparison for the SH. In general, the absolute
274 increase in OH is similar to that in the NH, both in observations and modeling, except
275 that at 60–70 km MLS observes in all cases larger absolute OH increase than in the
276 NH. The general agreement in OH change between the SIC EEP run and observations
277 is better in the SH. However, again on 30-May-2005 the model clearly overestimates the
278 OH concentration at all altitude between 65 and 75 km. Note that below 70 km, MLS
279 OH concentrations are generally higher than values predicted by the model, this was also
280 seen in some cases in the NH (Fig. 4). In all cases, the MLS EEP-peak-day OH profiles
281 agree better with the EEP run than with the CTR run (Table 3).

282 The increase in HO_x leads to significant depletion of mesospheric ozone, as already
283 shown in Fig. 3. The observed and modeled O₃ mixing ratios are shown in Fig. 6 for
284 two cases: January 2005, NH, and March 2005, SH. The notable difference between the
285 ozone altitude profiles is the tertiary ozone maximum around 75 km [e.g. Sofieva *et al.*,
286 2009, and references therein], which in our study is observed in January/NH but not in
287 March/SH. In both cases, modeled ozone depletion is seen at altitudes above 65 km after
288 the peak EEP days, but the March/SH changes are much smaller, because sunrise/sunset
289 OH increases are modest compared to January/NH (Fig. 3). The ozone results from
290 the EEP model run are in agreement with observations at most altitudes, indicating a
291 similar day-to-day variability with respect to EEP forcing. In January/NH, the maximum
292 depletion is observed at 75 km, where a decrease of about 0.4 ppmv is seen on January 3
293 and 4 compared to January 1, while there is a decrease of 0.5–0.6 ppmv in the EEP run
294 results with respect to January 1. By January 7, the EEP forcing has declined from
295 the peak values, and the ozone mixing ratios have returned close to the pre-EEP-peak

level. Compared to the CTR run results, those from the EEP run are clearly in better
agreement with the MLS observations. In March/SH at 75 km, ozone depletion of up to
0.1 ppmv is observed on March 8 and 9, compared to March 5. However, although the
EEP run results indicate a similar behavior, this change is smaller than the SEM of the
observations. Observing effects of this magnitude is obviously challenging.

4. Discussion

The SIC model is producing EEP-related OH changes that are comparable to those
observed by MLS, and the effects are seen at altitudes between 60–80 km, which is in
agreement with previous studies using only observations [Verronen *et al.*, 2011; Andersson
et al., 2012]. However, as shown in Fig. 1 the calculated ionization rates fall off rapidly
below 60 km, because of the applied 2 MeV upper limit for electron energies. As a result,
the calculated EEP impact might be somewhat underestimated in the lower mesosphere,
which could explain some of the OH underestimation in the model below 60 km. Although
it is possible that the same spectral form is applicable for energies higher than 2 MeV too,
the satellite-based electron data cannot be used to support or falsify this assumption.

The agreement between the modeled and observed OH response indicates that by intro-
ducing the daily average electron flux-energy spectra, based on MEPED and IDP electron
data, the EEP effect on the mesosphere can be modeled reasonably well. Note especially
that, in general, the EEP-related change on the peak EEP day (relative to the day before)
is overestimated also at lower altitudes (Tables 2 and 4), not underestimated. However, in
60–70% of the days shown in Figs. 4 and 5 the model tends to underestimate the observed
OH concentration (in absolute numbers) below 70 km, except in some cases where the
EEP ionization is very low (e.g. 12-April-2006, NH, Fig. 4). This could perhaps mean

318 that the assumed spectral form leads to too low electron fluxes at higher energies, and
 319 is consistent with the idea that an adjusting factor is required for higher energy electron
 320 precipitation (>300 keV electrons penetrate to altitudes below 70 km). Also, the fact that
 321 model-observation differences at <70 km altitudes occur also during moderate electron
 322 forcing is consistent with weak diffusion processes taking place in the radiation belts which
 323 will increase the satellite flux adjustment factor for >300 keV electrons during moderate
 324 forcing events [e.g. *Clilverd et al.*, 2012].

325 On the other hand, the fact that in Figs. 4 and 5 the model underestimation is some-
 326 times seen with low electron forcing (e.g. 5-March-2005 NH and 12-April-2006 SH) might
 327 also suggest a reason other than incorrect EEP fluxes. For example, there are also un-
 328 certainties related to, e.g., the assumption of angular distribution of electrons, and the
 329 additional ionization by Bremsstrahlung X-ray radiation produced by precipitating elec-
 330 trons is not considered (which would add to the ionization at the lower altitudes, below
 331 the main ionization peak, see e.g. *Schröter et al.* [2006]). Considering also that at lower
 332 altitudes the EEP effect is expected to be relatively small and that there is generally less
 333 OH (which makes the observation noisier), the overall agreement in OH is quite reason-
 334 able. Therefore, there seems to be no need for substantial (e.g. factor of 10) corrections
 335 to the electron flux observations, as suggested before [*Hendry et al.*, 2012; *Clilverd et al.*,
 336 2012], at least not in the energy range corresponding to the OH changes at 70–80 km.
 337 As a test, we multiplied the calculated electron flux values at all energies by a factor of
 338 10 and repeated the modeling for case of the March, 2005. The elevated fluxes resulted
 339 in significantly higher OH values from the model (not shown), with average difference
 340 between model and the observations at 60–78 km reaching 500%. This is obviously a poor

341 agreement compared to that between the observations and the original EEP model results
342 (Table 3).

343 As shown in Figs. 3 and 6, EEP events can cause short-term depletion of tens of
344 percent in mesospheric ozone. These changes are similar to those caused by large SPEs,
345 although having a somewhat smaller magnitude. For example, during the SPE of January
346 18, 2005, ozone was depleted by up to 90% at 70–80 km [e.g. *Verronen et al.*, 2006]. In
347 our study, the largest ozone effect was seen in the NH for the January 2005 case. This
348 is in agreement with previous studies of SPEs that have reported relatively larger ozone
349 response in the winter pole, related to the hemispheric differences in background HO_x
350 concentration [*Rohen et al.*, 2005; *Jackman et al.*, 2008; *Damiani et al.*, 2010].

351 In a recent study, mesospheric hydroxyl observations from August 2004 to Decem-
352 ber 2009 indicated an observable response to EEP in 22 (34%) of the 65 months
353 analyzed [*Andersson et al.*, 2012]. During the same time period, 13 SPEs of vari-
354 ous magnitudes took place according to the NOAA Space Weather Prediction Center
355 (<http://www.swpc.noaa.gov/ftplib/indices/SPE.txt>, accessed in January 2013). Assum-
356 ing that all 13 SPEs had an impact on the mesospheric OH concentrations, the rate of
357 large-enough EEP events exceeds the rate of hydroxyl-affecting SPEs by 70% during this
358 time period. Therefore, it is reasonable to argue that on time scales of a solar cycle, the
359 EEP forcing could be more important to mesospheric OH and ozone than SPEs. Obvi-
360 ously, longer time series of data, preferably covering several solar cycles, would be needed
361 for more quantitative conclusions.

5. Summary

362 We have used a 1-D ion and neutral chemistry model to study the effects of radiation
363 belt electron precipitation in the middle atmosphere. We considered four events, each
364 with high daily fluxes of precipitating electrons observed in the outer radiation belt. For
365 the modeling, the energy-flux spectra of electrons, and subsequently the atmospheric
366 ionization rates, were calculated based on electron observations of the MEPED and IDP
367 satellite instruments.

368 The model results show that the energetic electron precipitation can have a signifi-
369 cant effect on mesospheric OH and ozone. The maximum OH increase can reach several
370 hundred percent, but the magnitude of the relative effect depends strongly on the solar
371 zenith angle and the level of background OH production. Largest relative OH increases
372 are seen in the winter pole and around sunrise. The OH enhancements lead to ozone
373 depletion by up to several tens of percent, which is comparable to the effects previously
374 reported in cases of large SPEs. In general, the model is able to reproduce the observed
375 daily variability of OH and ozone, particularly at 70–80 km altitudes, although there are
376 significant differences in absolute OH concentrations in the lower mesosphere. Some of
377 the differences can be related to the assumptions made in the calculation of the electron
378 spectra and atmospheric ionization rates. Nevertheless, the general agreement between
379 the model and the observations indicate that the electron flux observations from satellites
380 for energies < 300 keV can be used to model the atmospheric effects of EEP at 70–80 km,
381 without a need for significant geometrical corrections. Some correction may be needed for
382 energies > 300 keV, although at lower altitudes we cannot make any strong conclusion
383 based on the current results.

384 **Acknowledgments.** The work of P.T.V. and M.E.A was supported by the Academy
385 of Finland through the projects #136225 and #140888 (SPOC: Significance of Energetic
386 Electron Precipitation to Odd Hydrogen, Ozone, and Climate). C.J.R. was supported by
387 the New Zealand Marsden fund. Research at the Jet Propulsion Laboratory, California
388 Institute of Technology, is performed under contract with the National Aeronautics and
389 Space Administration.

References

- 390 Andersson, M. E., P. T. Verronen, S. Wang, C. J. Rodger, M. A. Clilverd, and B. Carson
391 (2012), Precipitating radiation belt electrons and enhancements of mesospheric hydroxyl
392 during 2004-2009, *J. Geophys. Res.*, *117*, D09,304, doi:10.1029/2011JD017246.
- 393 Clilverd, M. A., et al. (2010), Ground-based estimates of outer radiation belt energetic
394 electron precipitation fluxes into the atmosphere, *J. Geophys. Res.*, *115*, A12304, doi:
395 10.1029/2010JA015638.
- 396 Clilverd, M. A., C. J. Rodger, D. Danskin, M. E. Usanova, T. Raita, T. Ulich, and
397 E. L. Spanswick (2012), Energetic particle injection, acceleration, and loss during the
398 geomagnetic disturbances which upset Galaxy 15, *J. Geophys. Res.*, *117*, A12,213, doi:
399 10.1029/2012JA018175.
- 400 Damiani, A., M. Storini, M. Laurenza, and C. Rafanelli (2008), Solar particle effects on
401 minor components of the Polar atmosphere, *Ann. Geophys.*, *26*, 361–370.
- 402 Damiani, A., M. Storini, C. Rafanelli, and P. Diego (2010), The hydroxyl radical as an
403 indicator of SEP fluxes in the high-latitude terrestrial atmosphere, *Adv. Space Res.*, *46*,
404 1225–1235, doi:10.1016/j.asr.2010.06.022.

- 405 Evans, D. S., and M. S. Greer (2004), Polar orbiting environmental satellite space envi-
 406 ronment monitor – 2 instrument descriptions and archive data documentation, NOAA
 407 Technical Memorandum version 1.4, Space Environment Laboratory, Colorado.
- 408 Goldberg, R. A., C. H. Jackman, J. R. Barcus, and F. Soraas (1984), Nighttime auroral
 409 energy deposition in the middle atmosphere, *J. Geophys. Res.*, *89*, 5581–5596.
- 410 Grenfell, J. L., R. Lehmann, P. Mieth, U. Langematz, and B. Steil (2006), Chemical
 411 reaction pathways affecting stratospheric and mesospheric ozone, *J. Geophys. Res.*, *111*,
 412 D17,311, doi:10.1029/2004JD005713.
- 413 Heaps, M. G. (1978), The effect of a solar proton event on the minor neutral constituents
 414 of the summer polar mesosphere, *Tech. Rep. ASL-TR0012*, U.S. Army Atmos. Sci. Lab.,
 415 White Sands Missile Range, N. M.
- 416 Hedin, A. E. (1991), Extension of the MSIS thermospheric model into the middle and
 417 lower atmosphere, *J. Geophys. Res.*, *96*, 1159–1172.
- 418 Hendry, A. T., C. J. Rodger, M. A. Clilverd, N. R. Thomson, S. K. Morley, and T. Raita
 419 (2012), Rapid radiation belt losses occurring during high speed solar wind stream driven
 420 storms: importance of energetic electron precipitation, in *Dynamics of the Earth’s Ra-*
 421 *diation Belts and Inner Magnetosphere*, *American Geophysical Union Monograph*, vol.
 422 199, edited by D. Summers, I. R. Mann, D. N. Baker, and M. Schulz, pp. 213–223,
 423 American Geophysical Union, doi:10.1029/2012GM001299.
- 424 Jackman, C. H., et al. (2008), Short- and medium-term atmospheric constituent effects
 425 of very large solar proton events, *Atmos. Chem. Phys.*, *8*, 765–785, doi:10.5194/acp-8-
 426 765-2008.

- 427 Jiang, Y. B., et al. (2007), Validation of Aura Microwave Limb Sounder ozone
428 by ozonesonde and lidar measurements, *J. Geophys. Res.*, *112*, D24S34, doi:
429 10.1029/2007JD008776.
- 430 Livesey, N. J., et al. (2011), EOS MLS Version 3.3 Level 2 data quality and description
431 document, JPL D-33509, Jet Propulsion Laboratory, Version 3.3x-1.0, January 18.
- 432 Pickett, H. M., W. G. Read, K. K. Lee, and Y. L. Yung (2006), Observation of night OH
433 in the mesosphere, *Geophys. Res. Lett.*, *33*, L19,808, doi:10.1029/2006GL026910.
- 434 Pickett, H. M., et al. (2008), Validation of Aura Microwave Limb Sounder OH and HO₂
435 measurements, *J. Geophys. Res.*, *113*, D16S30, doi:10.1029/2007JD008775.
- 436 Rees, M. H. (1989), *Physics and chemistry of the upper atmosphere*, Cambridge atmo-
437 spheric and space science series, Cambridge University Press, Cambridge, UK.
- 438 Rodger, C. J., M. A. Clilverd, J. C. Green, and M. M. Lam (2010a), Use of POES SEM-2
439 observations to examine radiation belt dynamics and energetic electron precipitation
440 into the atmosphere, *J. Geophys. Res.*, *115*, A04,202, doi:10.1029/2008JA014023.
- 441 Rodger, C. J., B. R. Carson, S. A. Cummer, R. J. Gamble, M. A. Clilverd, J.-A. Sauvaud,
442 M. Parrot, J. C. Green, and J.-J. Berthelier (2010b), Contrasting the efficiency of
443 radiation belt losses caused by ducted and non-ducted whistler mode waves from ground-
444 based transmitters, *J. Geophys. Res.*, *115*, A12,208, doi:10.1029/2010JA015880.
- 445 Rohen, G., et al. (2005), Ozone depletion during the solar proton events of Octo-
446 ber/November 2003 as seen by SCIAMACHY, *J. Geophys. Res.*, *110*, A09S39.
- 447 Sauvaud, J. A., et al. (2006), High-energy electron detection onboard DEMETER: The
448 IDP spectrometer, description and first results on the inner belt, *Planet. Space Sci.*, *54*,
449 502–511.

- 450 Schröter, J., B. Heber, F. Steinhilber, and M. Kallenrode (2006), Energetic particles
 451 in the atmosphere: A Monte-carlo simulation, *Adv. Space Res.*, *37*, 1597–1601, doi:
 452 10.1016/j.asr.2005.05.085.
- 453 Sofieva, V. F., et al. (2009), Spatio-temporal observations of the tertiary ozone maximum,
 454 *Atmos. Chem. Phys.*, *9*, 4439–4445, doi:10.5194/acp-9-4439-2009.
- 455 Solomon, S., D. W. Rusch, J.-C. Gérard, G. C. Reid, and P. J. Crutzen (1981), The
 456 effect of particle precipitation events on the neutral and ion chemistry of the middle
 457 atmosphere: II. Odd hydrogen, *Planet. Space Sci.*, *8*, 885–893.
- 458 Tobiska, W. K., T. Woods, F. Eparvier, R. Viereck, L. D. B. Floyd, G. Rottman, and
 459 O. R. White (2000), The SOLAR2000 empirical solar irradiance model and forecast
 460 tool, *J. Atmos. Sol.-Terr. Phys.*, *62*, 1233–1250.
- 461 Turunen, E., P. T. Verronen, A. Seppälä, C. J. Rodger, M. A. Clilverd, J. Tamminen,
 462 C.-F. Enell, and T. Ulich (2009), Impact of different precipitation energies on NO_x
 463 generation during geomagnetic storms, *J. Atmos. Sol.-Terr. Phys.*, *71*, 1176–1189, doi:
 464 10.1016/j.jastp.2008.07.005.
- 465 Verronen, P. T. (2006), *Ionosphere-atmosphere interaction during solar proton events*,
 466 no. 55 in Finnish Meteorological Institute Contributions, Finnish Meteorological Insti-
 467 tute, Helsinki, Finland, URL: <http://urn.fi/URN:ISBN:952-10-3111-5>.
- 468 Verronen, P. T., and R. Lehmann (2013), Analysis and parameterisation of ionic reactions
 469 affecting middle atmospheric HO_x and NO_y during solar proton events, *Ann. Geophys.*,
 470 *31*, 909–956, doi:10.5194/angeo-31-909-2013.
- 471 Verronen, P. T., A. Seppälä, M. A. Clilverd, C. J. Rodger, E. Kyrölä, C.-F. Enell,
 472 T. Ulich, and E. Turunen (2005), Diurnal variation of ozone depletion during the

473 October-November 2003 solar proton events, *J. Geophys. Res.*, *110*, A09S32, doi:
474 10.1029/2004JA010932.

475 Verronen, P. T., A. Seppälä, E. Kyrölä, J. Tamminen, H. M. Pickett, and E. Turunen
476 (2006), Production of odd hydrogen in the mesosphere during the January 2005 solar
477 proton event, *Geophys. Res. Lett.*, *33*, L24,811, doi:10.1029/2006GL028115.

478 Verronen, P. T., C. J. Rodger, M. A. Clilverd, and S. Wang (2011), First evidence of
479 mesospheric hydroxyl response to electron precipitation from the radiation belts, *J.*
480 *Geophys. Res.*, *116*, D07,307, doi:10.1029/2010JD014965.

481 Waters, J. W., et al. (2006), The Earth Observing System Microwave Limb Sounder
482 (EOS MLS) on the Aura satellite, *IEEE Trans. Geosci. Remote Sens.*, *44*, 1075–1092,
483 doi:10.1109/TGRS.2006.873771.

484 _____

Table 1. Details of the monthly cases. RD = the day-before reference day used when calculating observed and modeled changes. For all modeling locations, the geomagnetic latitude is about 60°.

Month	Modeling period (day)	Modeling locations (geographic)	EEP peak day (day)	RD (day)	Number of MLS profiles (NH/SH)
January 2005	01 – 10	60°N/0°E, 50°S/105°E	02	01	57–68/18–24
March 2005	05 – 10	60°N/0°E, 65°S/0°E	07	05	95–105/52–69
May 2005	25 – 31	55°N/75°W, 65°S/0°E	30	29	13–19/97–112
April 2006	13 – 17	60°N/0°E, 65°S/0°E	14	12	20–33/72–84

Table 2. Northern Hemisphere: observed (MLS) and modeled (SIC) OH changes caused by the peak EEP day forcing. Both absolute (in units 10^5 cm^{-3}) and relative changes (in brackets) are shown. Columns from left to right: 1) EEP peak day, 2) observed mean change at 60–70 km, 3) observed mean change at 71–81 km, 4) modeled mean change at 60–70 km, and 5) modeled mean change at 71–81 km. The SIC changes (columns 4 and 5) are calculated from the EEP run results. Both SIC and MLS changes are relative to the day before, as indicated in Table 1 (reference day). The SEM of the MLS numbers varies between 15 and 45%.

	MLS	MLS	SIC	SIC
Alt (km)	60–70	71–81	60–70	71–81
02-Jan-2005	0.8 (24%)	6.0 (70%)	1.5 (67%)	6.1 (65%)
07-Mar-2005	1.6 (67%)	7.2 (108%)	4.7 (240%)	8.5 (200%)
30-May-2005	-2.1 (-30%)	2.6 (34%)	5.5 (94%)	12.7 (140%)
14-Apr-2006	0.7 (55%)	10.9 (266%)	5.1 (179%)	14.4 (240%)

Table 3. Differences between modeled (CTR and EEP runs) and observed (MLS) OH concentrations, averaged between 60–78 km. Absolute differences are calculated as $\text{abs}(\text{SIC} - \text{MLS})$ and relative differences as $100 \times (\text{SIC}/\text{MLS} - 1)$. For each month, the upper line is for NH and the lower line for SH.

		CTR vs. MLS	EEP vs. MLS
		10^5 cm^{-3} (%)	10^5 cm^{-3} (%)
02-Jan-2005	NH	4.7 (−59)	1.2 (−11)
	SH	8.1 (−23)	6.3 (+8)
07-Mar-2005	NH	5.3 (−54)	3.1 (+44)
	SH	6.6 (−52)	3.7 (−17)
30-May-2005	NH	3.7 (+46)	8.0 (+219)
	SH	3.8 (−47)	2.5 (−10)
14-Apr-2006	NH	4.8 (−40)	4.5 (+70)
	SH	4.5 (−45)	2.4 (−12)

Table 4. Like Table 2 but for Southern Hemisphere.

	MLS	MLS	SIC	SIC
Alt (km)	60–70	71–81	60–70	71–81
02-Jan-2005	3.7 (53%)	-1.5 (-17%)	1.7 (30%)	4.1 (33%)
07-Mar-2005	3.6 (94%)	8.9 (124%)	2.7 (65%)	7.8 (77%)
30-May-2005	2.1 (50%)	6.7 (73%)	7.5 (190%)	12.4 (70%)
14-Apr-2006	2.2 (69%)	6.4 (81%)	3.5 (130%)	8.1 (69%)

Figure 1. Left: EEP flux-energy spectra on selected days in January 2005. Right: corresponding, calculated atmospheric ionization rate profiles for the NH modeling location.

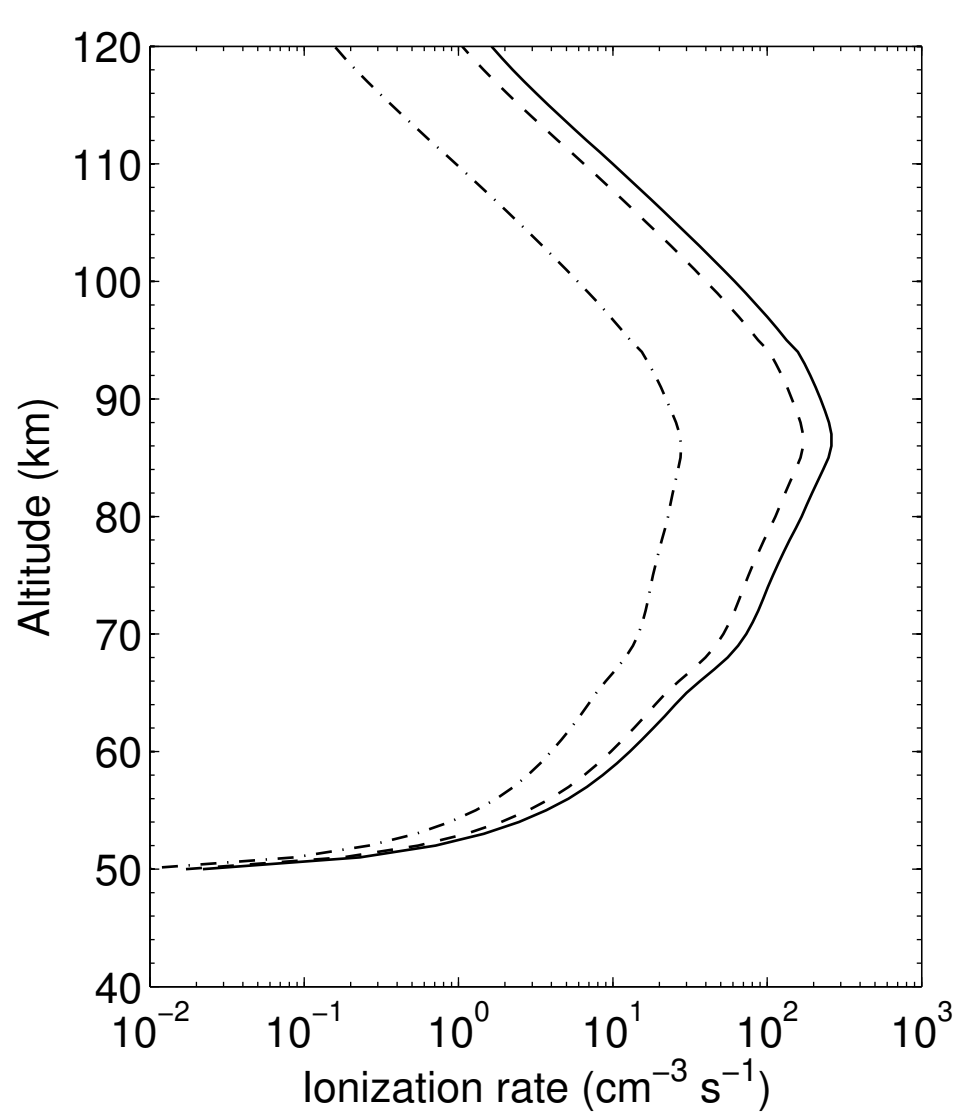
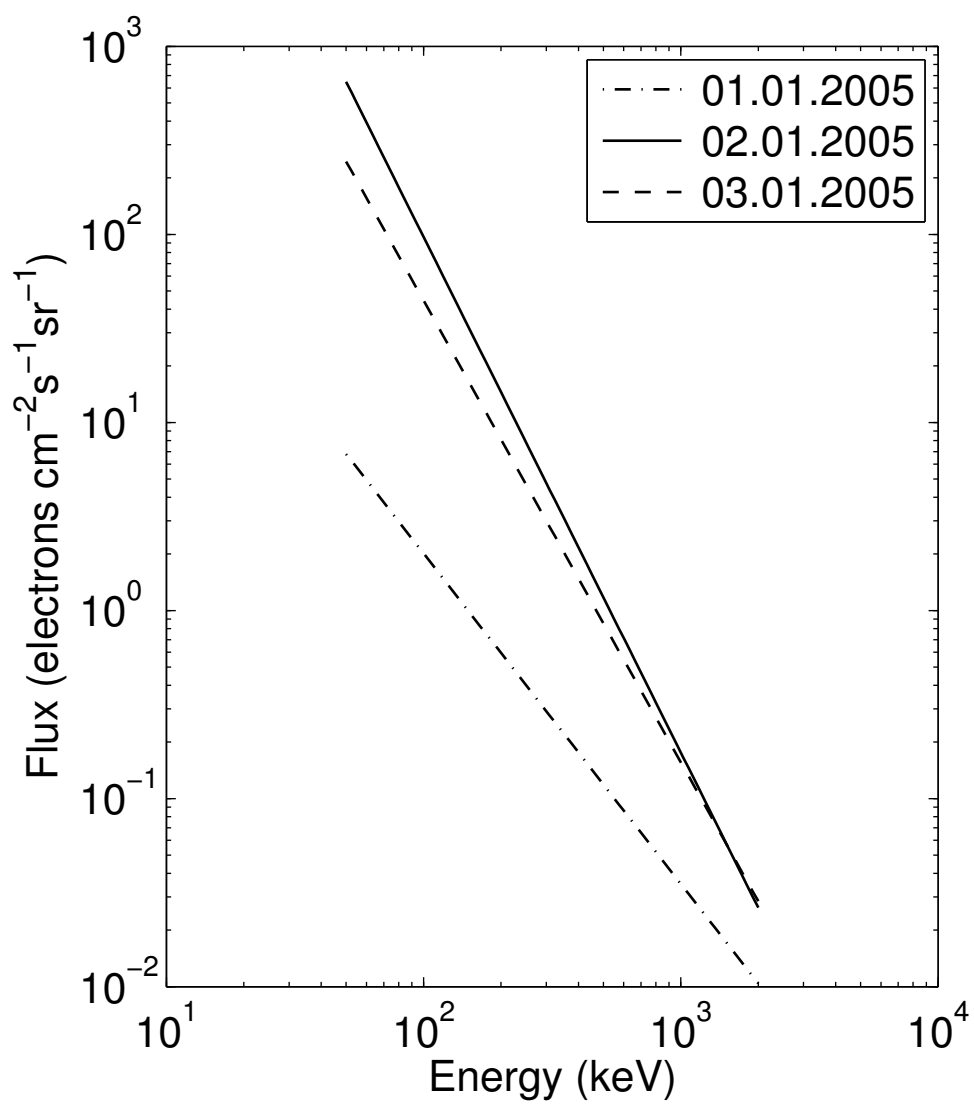
Figure 2. Calculated daily-mean EEP ionization rates at selected altitudes for the NH modeling locations.

Figure 3. Comparison between modeled and observed EEP-caused relative change of OH and ozone at about 75 km for January NH (left) and March SH (right) 2005. Red line: SIC data showing $100 \times (\text{EEP}/\text{CTR} - 1)$, where EEP and CTR are gas concentrations from the electron and control runs, respectively. Red X marks: Same as Red Line, except that CTR is replaced by 1st-day result from the EEP run, and shown only at the LST of MLS observations. Blue circles: MLS data showing the change with respect to the observations on the day before EEP peak (see Table 1). Gray shading marks the local times with solar zenith angle larger than 100° , i.e. approximative nighttime.

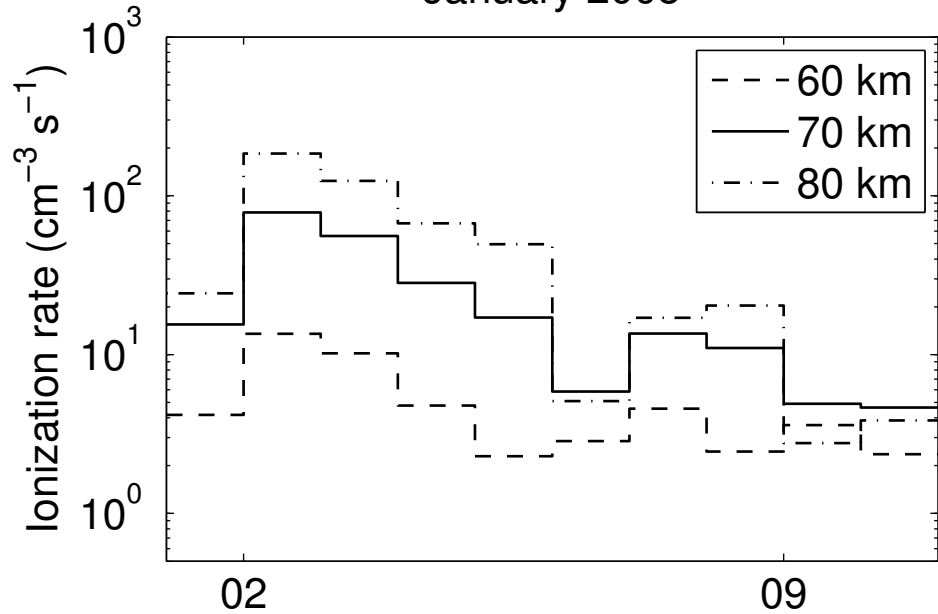
Figure 4. Comparison of NH modeled and observed nighttime OH concentrations before (left), during (middle), and after (right) the peak EEP day. Rows from top down: January 2005, March 2005, May 2005, and April 2006. Black, red, and blue colors mark data from SIC CTR run, SIC EEP run, and MLS observations, respectively.

Figure 5. Like Fig. 4 but for SH.

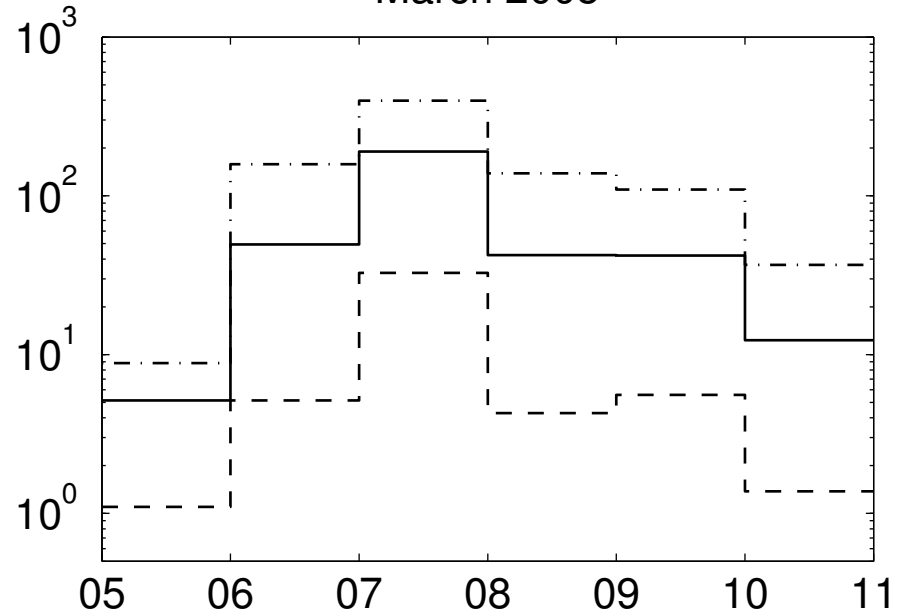
Figure 6. Comparison of modeled and observed nighttime ozone mixing ratios. Top row: January 2005, NH. Bottom row: March 2005, SH. Black, red, and blue colors mark data from SIC CTR run, SIC EEP run, and MLS observations, respectively.



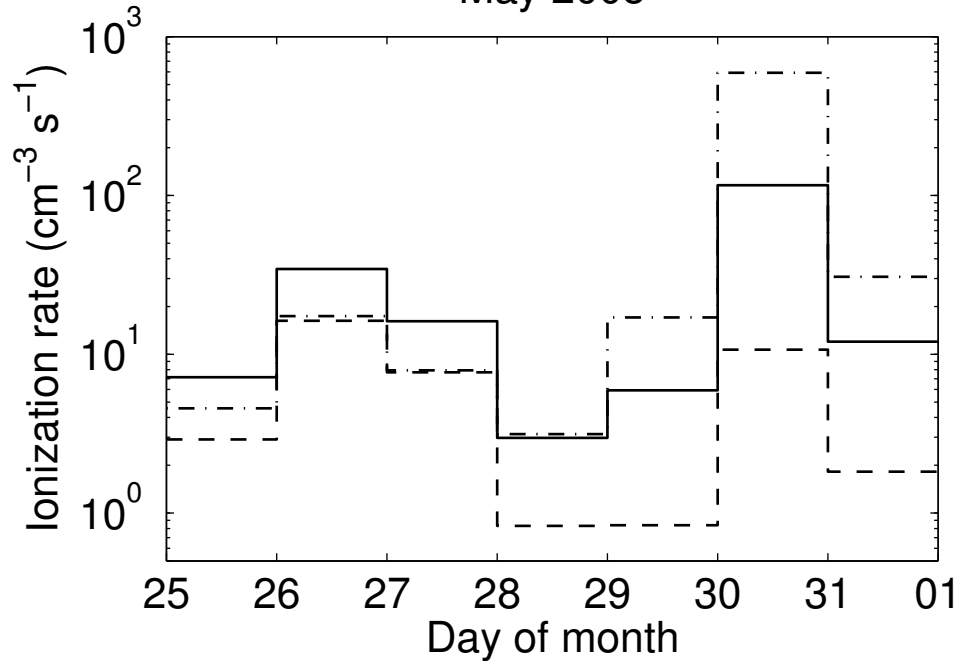
January 2005



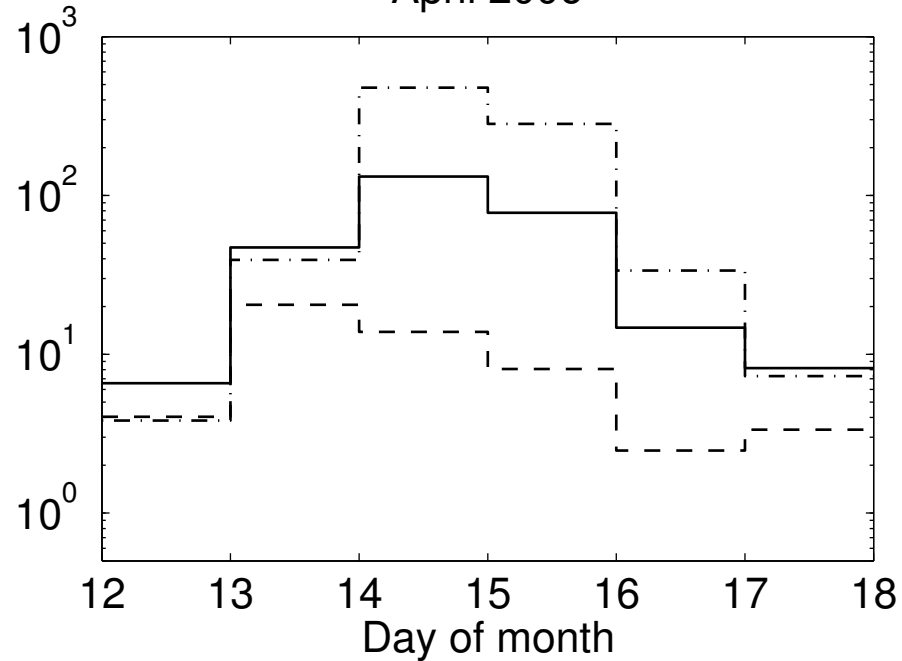
March 2005



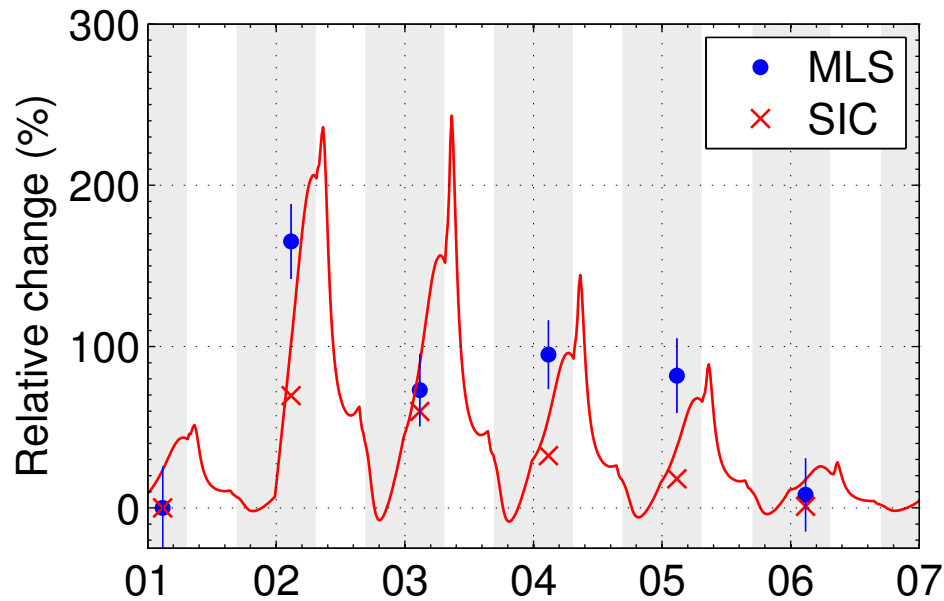
May 2005



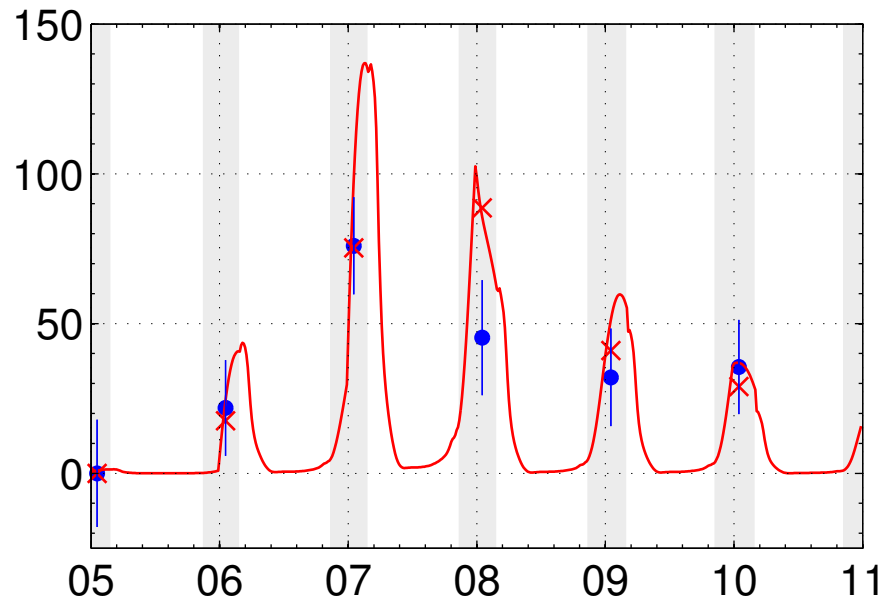
April 2006



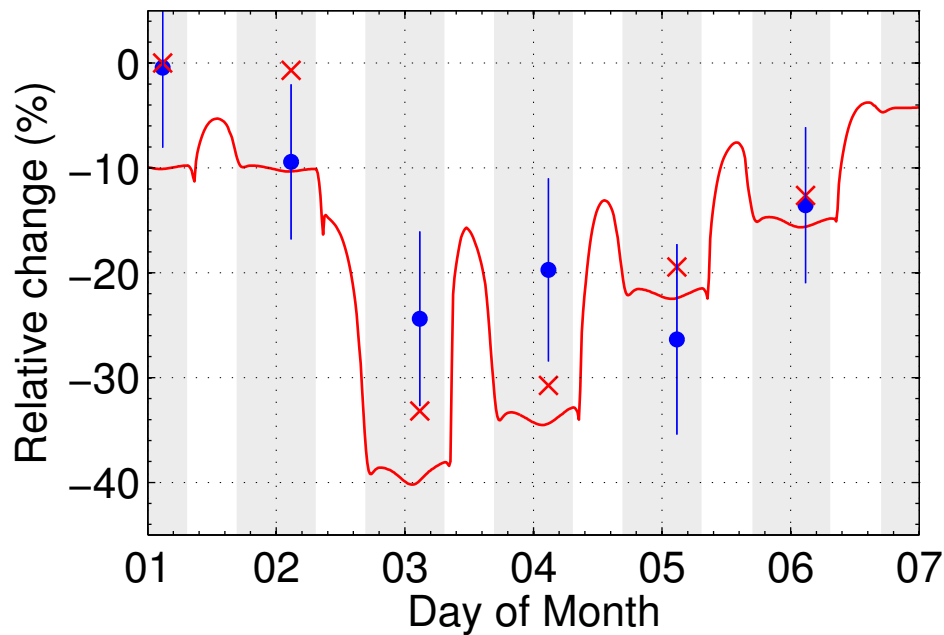
OH, NH, January 2005, 74 km



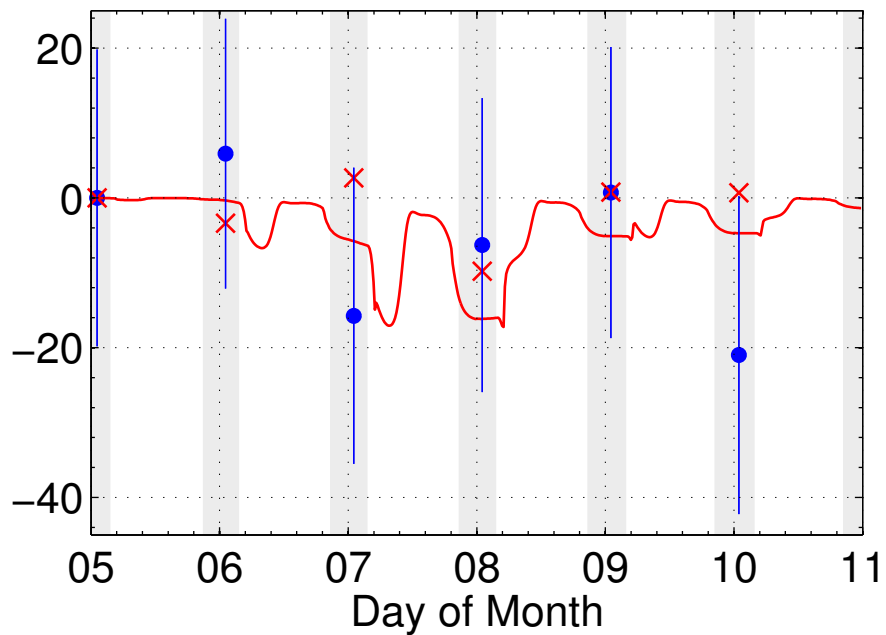
OH, SH, March 2005, 74 km



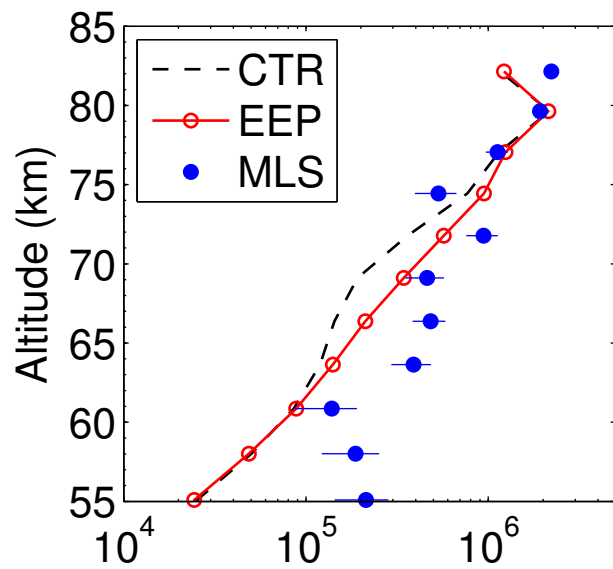
Ozone, NH, January 2005, 74 km



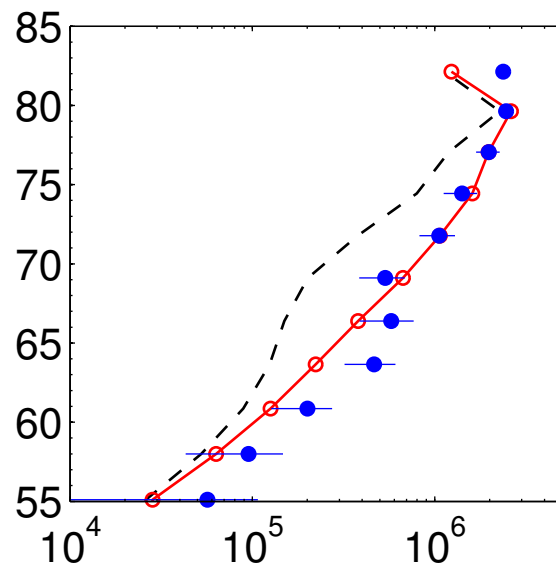
Ozone, SH, March 2005, 76 km



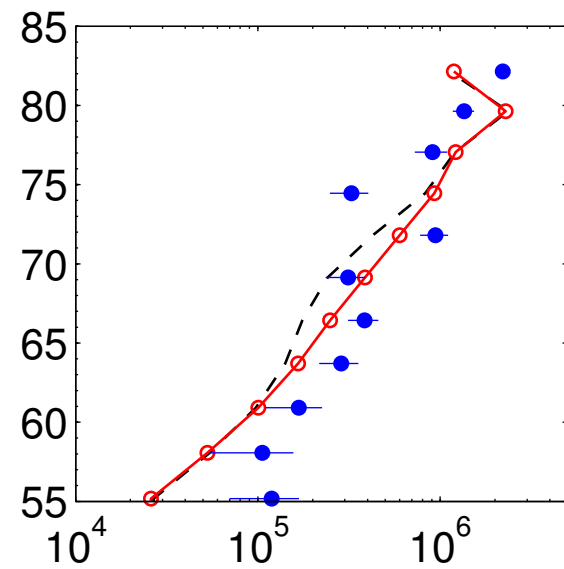
01-Jan-2005



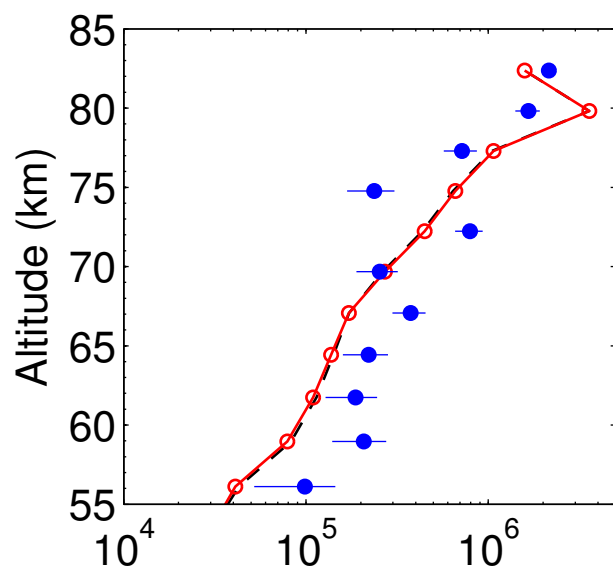
02-Jan-2005



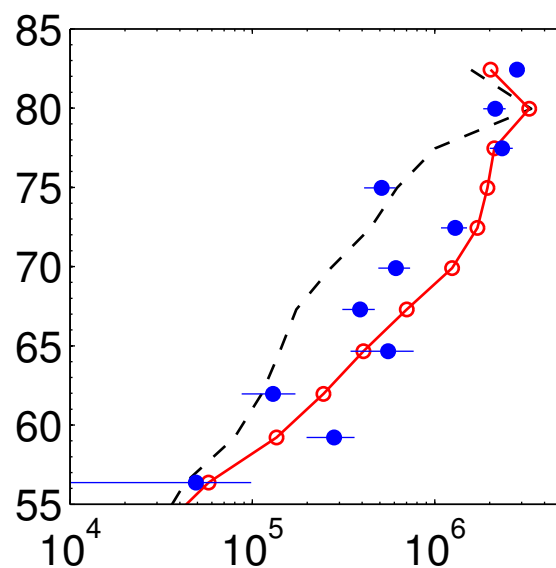
09-Jan-2005



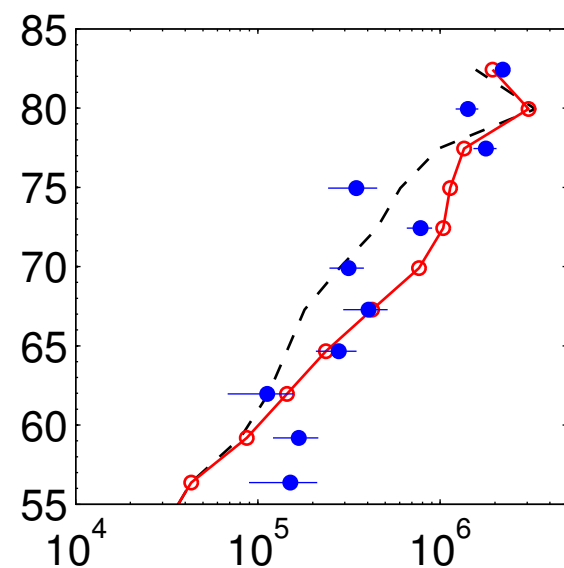
05-Mar-2005



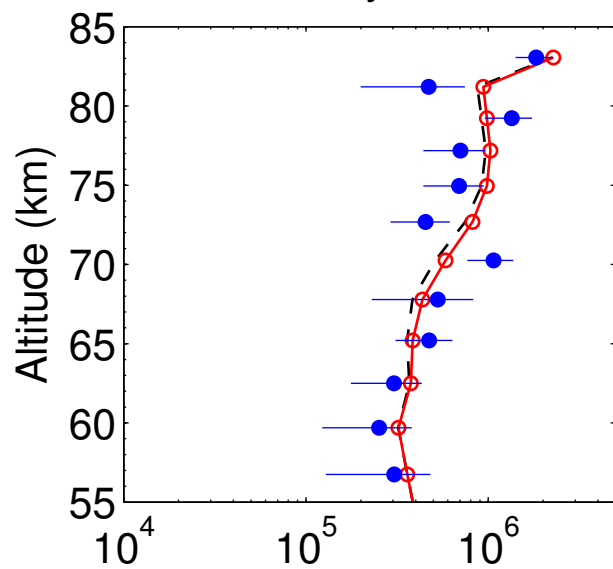
07-Mar-2005



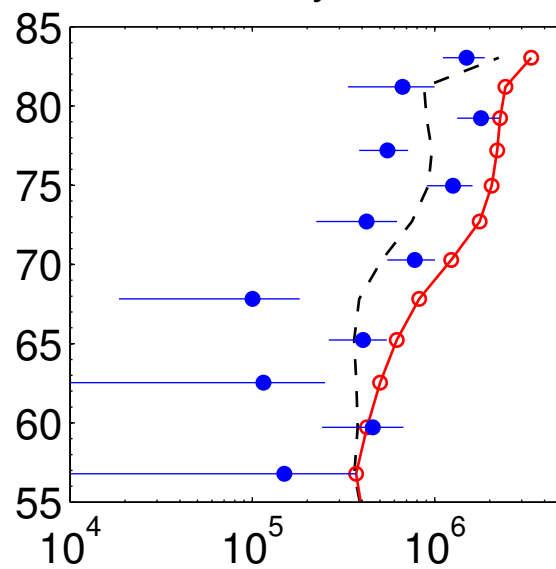
09-Mar-2005



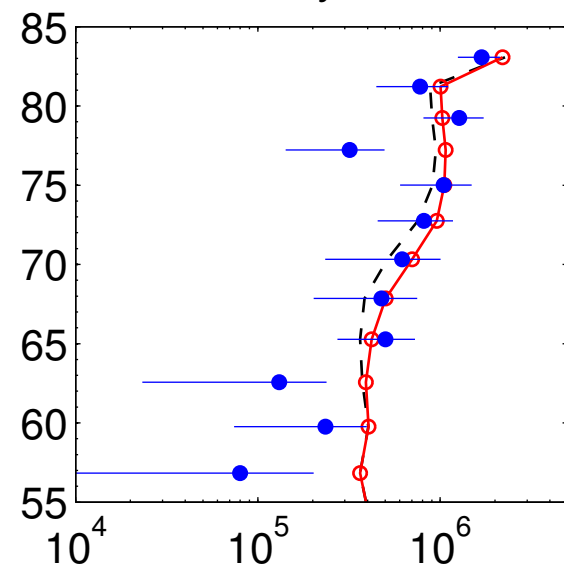
29-May-2005



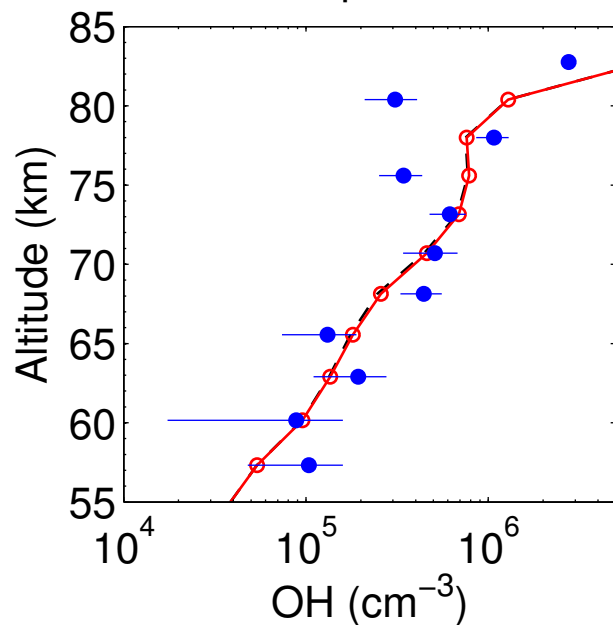
30-May-2005



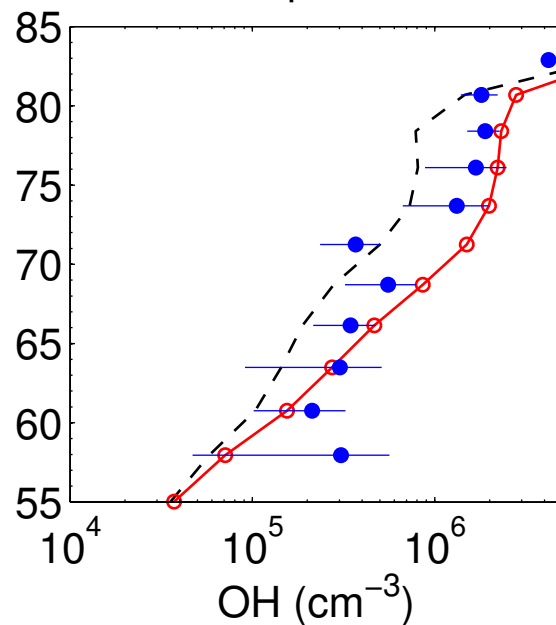
31-May-2005



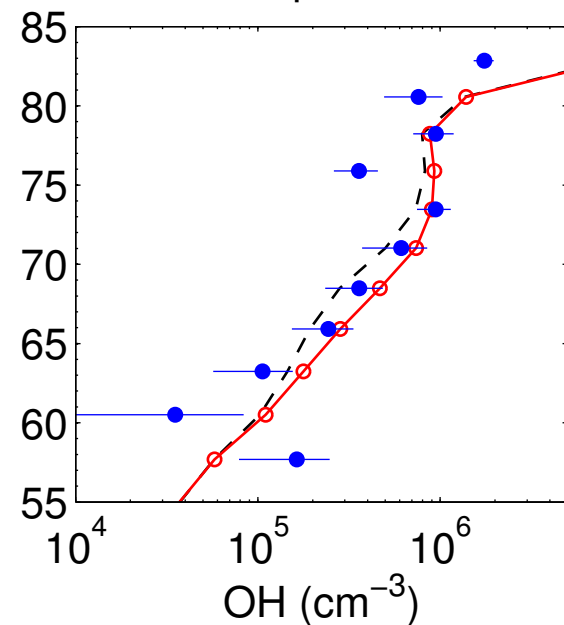
12-Apr-2006



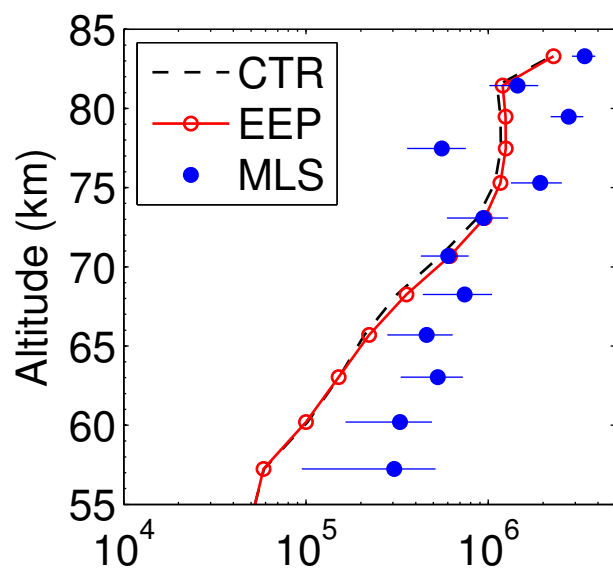
14-Apr-2006



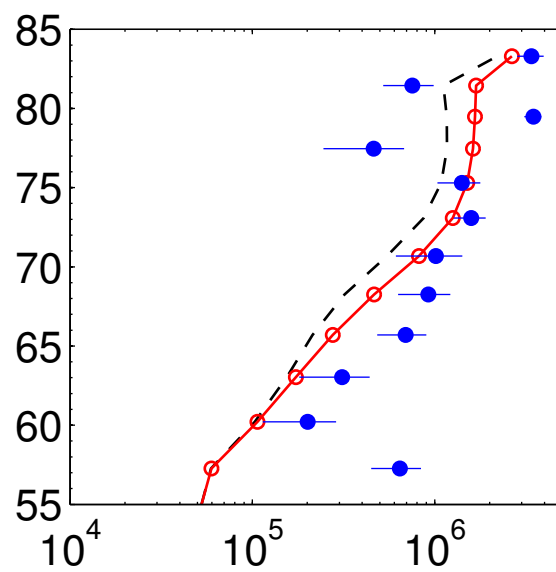
17-Apr-2006



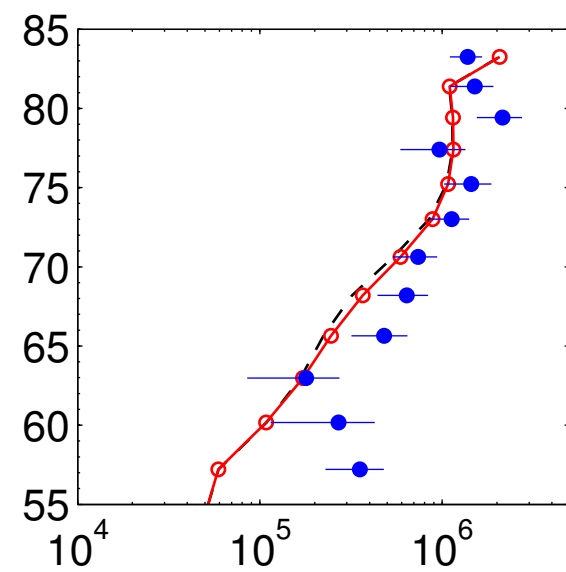
01-Jan-2005



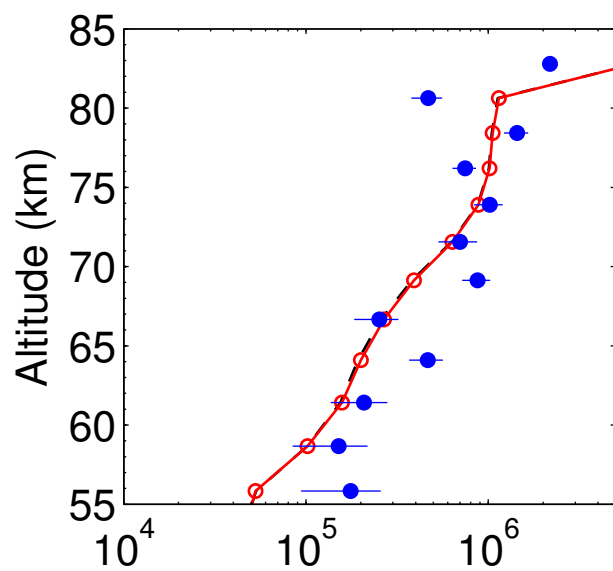
02-Jan-2005



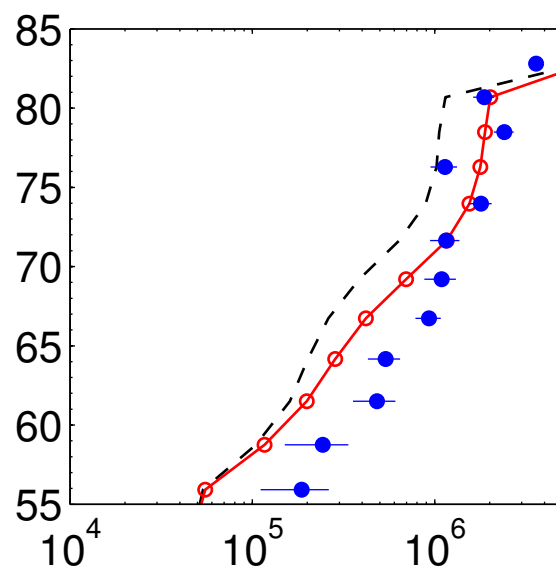
09-Jan-2005



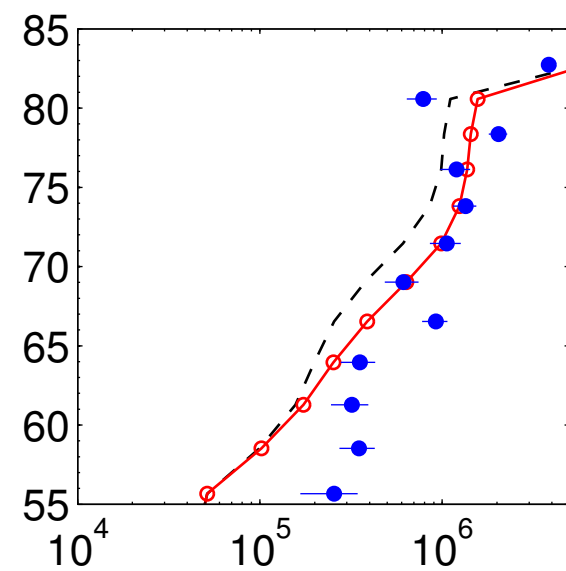
05-Mar-2005



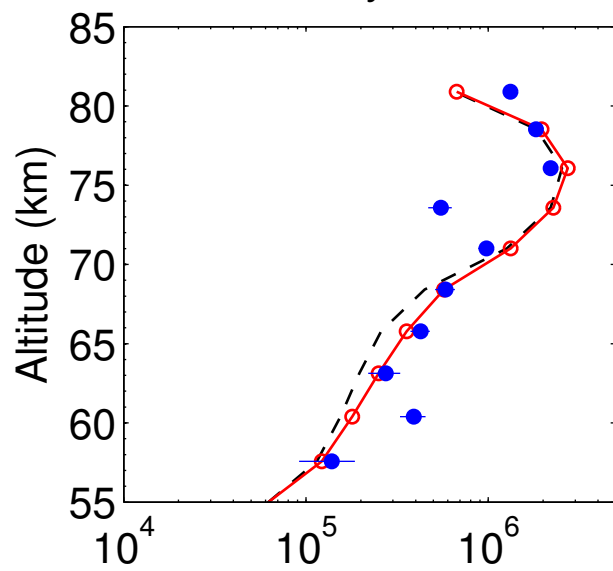
07-Mar-2005



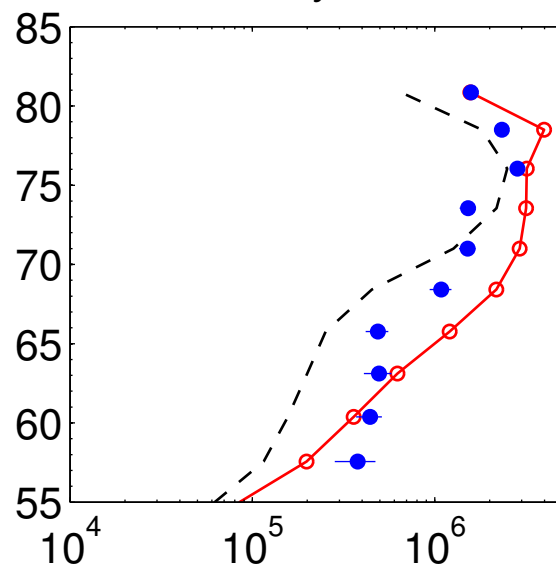
09-Mar-2005



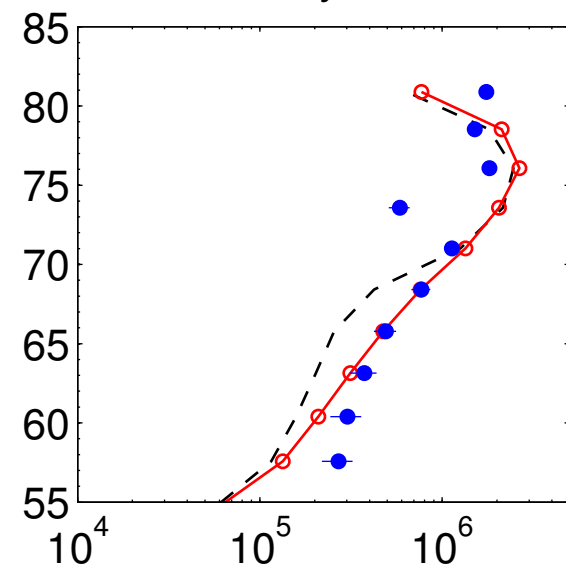
29-May-2005



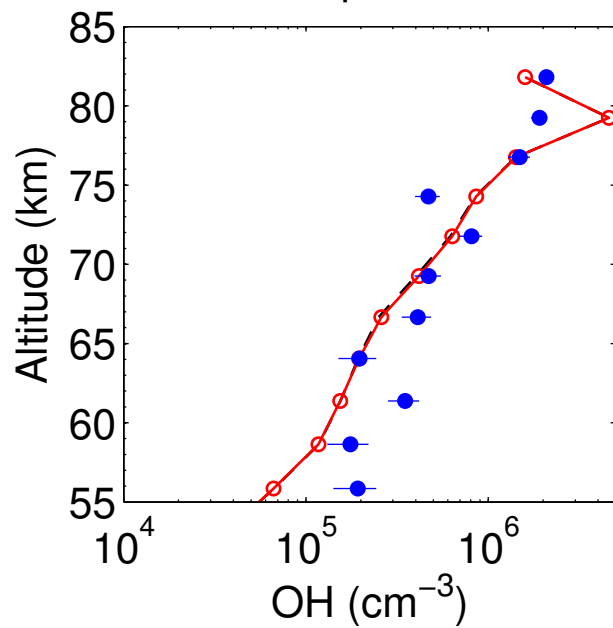
30-May-2005



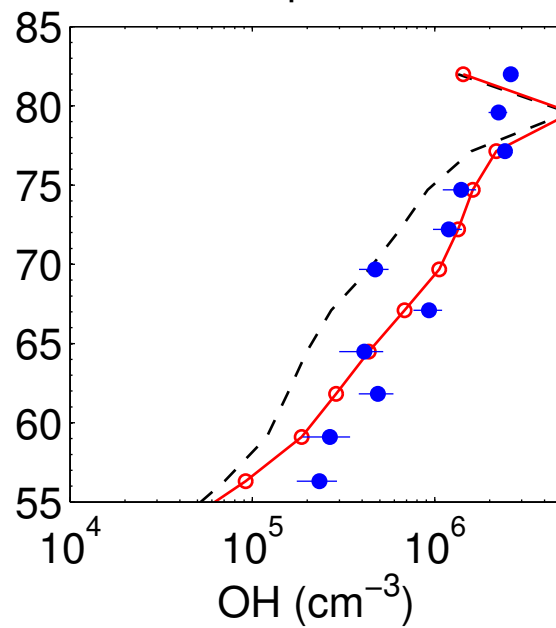
31-May-2005



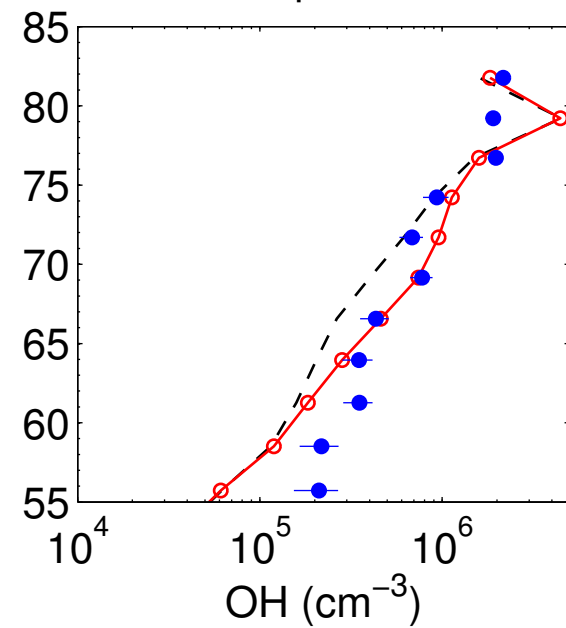
12-Apr-2006



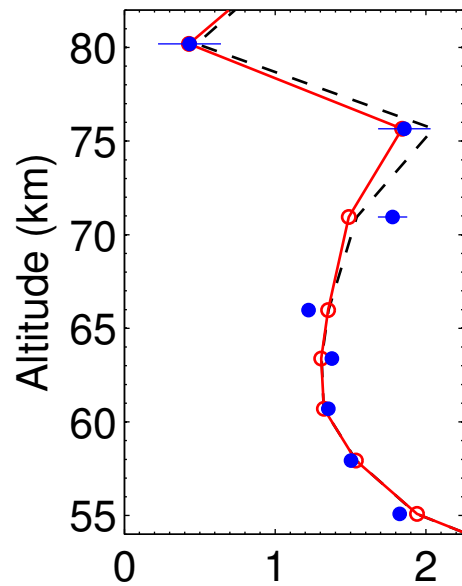
14-Apr-2006



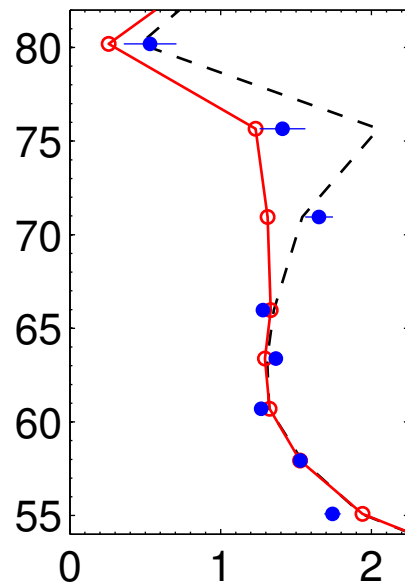
17-Apr-2006



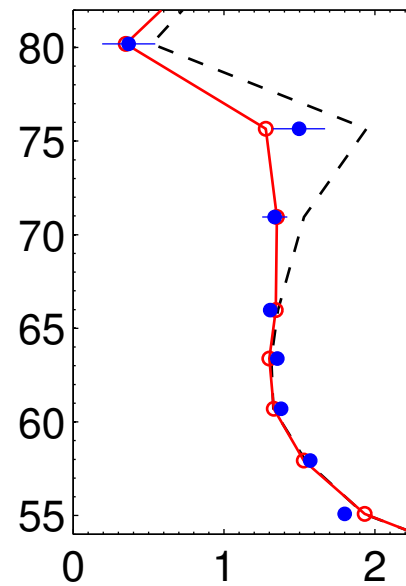
01-Jan-2005



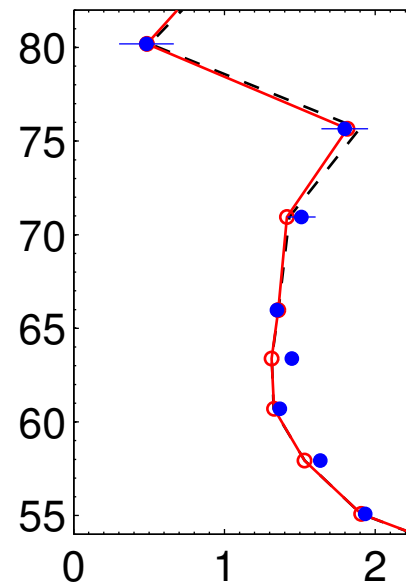
03-Jan-2005



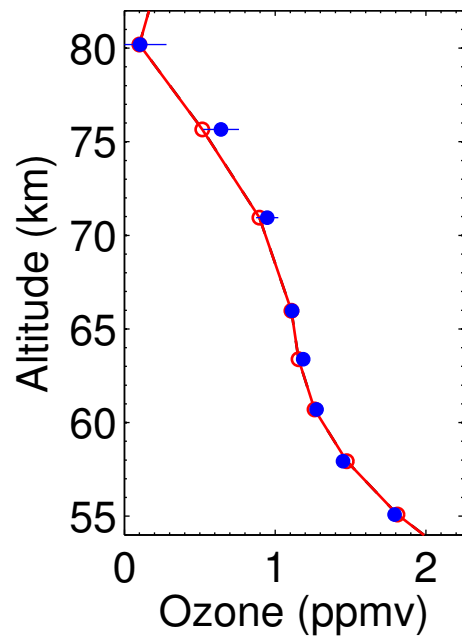
04-Jan-2005



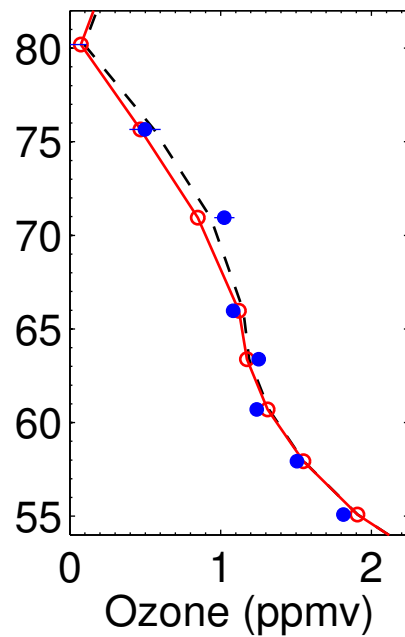
07-Jan-2005



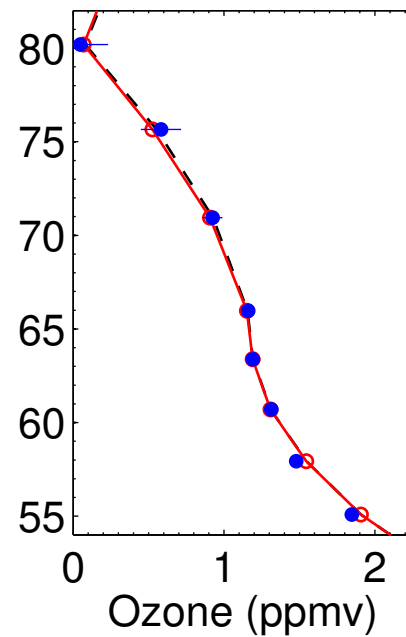
05-Mar-2005



08-Mar-2005



09-Mar-2005



10-Mar-2005

